Available online at www.sdcjter.in

SDC Journal of Theoretical and Experimental Research (SDCJTER) 01(02), 2023, 19 –35

Effect of RF power on the structural, morphological and optical properties of RF sputtered zinc oxide thin films

Sreeja Sreedharan. R[a,b*]

[a]*Department of Physics, Sanatana Dharma College, University of Kerala, Alappuzha, 688 003, Kerala, India.*
[b]*Department of Optoeiectronics, University of Kerala, Kariavattom, 695 581, Kerala, India*

Available online 01 June 2023

Abstract

The properties of the sputtered films are highly influenced by the preparation conditions. An attempt is made to optimize the preparation conditions of RF sputtered ZnO films in terms of RF power. The structural, morphological and optical properties of the films were studied to investigate the influence of RF power on the crystalline quality, surface morphology, transmittance and luminescent properties of sputtered films.

© 2023 Published by Sanatana Dharma College, Alappuzha.

Keywords: Sputtering, XRD, Micro-Raman Spectroscopy, Spectroscopic Ellipsometry

1. Introduction

ZnO is a direct band gap II-VI semiconductor. It has a large exciton binding energy of 60 meV (at room temperature), whereas most of the commonly used semiconductors in the industry such as ZnSe and GaN have relatively lower values for binding energy (22 meV and 25 meV respectively for ZnSe and GaN) [Ohshima et al.,2003]. ZnO generally exhibits two types of emissions: one is UV emission due to the near band edge transition and the other is the deep level visible emission due to defects in ZnO. The ratio of intensity of UV emission to visible emission can be taken as a criterion for evaluating the crystalline quality of the ZnO films [Irimpan et al., -2008]. Because of its variety of applications in various fields such as sensors [Pati et al., 2014], transparent electrodes for solar cells [Gonzalez, et al.,1998], UV emitting devices, [Cho et al., 1999] laser diodes [Maslov et al., 2004], etc. ZnO has received much attention in the semiconductor industry. Moreover it is a bio-safe and bio-compatible semiconductor material [Singh et al., 2015]. Different fabrication techniques such pulsed laser deposition (PLD) [Ryu et al., 2000], sputtering [Lua et al., 2001], molecular beam epitaxy (MBE) [Ko et al., 2000-1], metal organic chemical vapour deposition (MOCVD) [Kashiwaba et al., 2002], Sol-gel method [Natsume et al., 2000], spray pyrolysis, [Krunks et al., 1995] etc., can be used for the preparation of ZnO thin films. The films synthesized by physical methods generally possess better crystalline quality than the films synthesized by chemical solution deposition techniques [Wang et al., 2009]. Among the various thin film fabrication techniques, RF magnetron sputtering is treated as one of the versatile methods for the fabrication of

* Corresponding author: *Email address*: sreeja.sreedharan@sdcollege.in (Sreeja Sreedharan R)

high quality ZnO films due to the relatively high deposition rates at low operating temperature [Puchert et al., 1996] and the process can easily be extended to industrial production lines [Kappertz et al., 2002]. Usually high quality ZnO films are obtained by growing the films on heated substrates or by post-deposition annealing at high temperatures. Sputtering offers a relatively low temperature deposition technology for the growth of good quality pure and doped ZnO films without the use of in situ substrate heating or post-deposition annealing [Puchert et al., 1996]. For obtaining good quality films, the deposition parameters have to be optimized. In the present investigation, ZnO films were fabricated on quartz substrates at three different RF powers viz, 100, 150 and 200 W at room temperature. The films are characterized by techniques such as X-ray diffraction (XRD), micro-Raman spectroscopy, atomic force microscopy (AFM), field emission scanning electron microscopy (FESEM), spectroscopic ellipsometry, UV-visible and photoluminescence (PL) spectroscopy.

2. Experimental

ZnO thin films were fabricated on cleaned quartz substrates using RF magnetron sputtering technique. Commercially available ZnO powder (Aldrich make, purity-99.99%) was thoroughly ground using agate mortar and pestle.The pressed powder was used as the target for film preparation. The deposition was carried out at room temperature inside a vacuum chamber which is evacuated initially to a base pressure of 3×10^{-6} mbar using a diffusion pump backed by a rotary pump. Argon gas was then admitted in to the chamber and argon pressure was maintained at 0.02 mbar. The target was powered by a magnetron power supply (Advanced Energy, MDX 500) operating at a frequency of 13.56 MHz. The films were fabricated on cleaned quartz substrates kept at a distance of 5 cm from the target surface. The film deposition was carried out for a duration of 30 minutes for three different RF powers viz 100, 150 and 200 W. The as-prepared films deposited using RF powers of 100, 150 and 200 W were designated as W1, W2 and W3 respectively.

The X-ray diffraction patterns of the films were recorded in the 2θ range 10-70º in Bragg-Brentano geometry (angular step size 0.0203º and scan speed 2˚/min) by Bruker AXS D8 Advance X-ray diffractometer using Cu $K\alpha_1$ radiation of wavelength 1.5406Aº. The Raman spectra were recorded using an excitation radiation of wavelength 514.5 nm from an argon ion laser using Labram-HR 800. Micro-Raman spectrometer with 1 cm^{-1} spectral resolution. AFM measurements (Digital Instruments Nanoscope III) were carried out in contact mode (Si_3N_4 100μ cantilever having force constant 0.58 N/m) and the data were analyzed using WSxM 5.0 Develop 6.4 software. FESEM measurements were carried out using Nano SEM-450 (FEI-Nova Model No.1027647) equipped with XFlash detector 6/10 (Bruker). The elemental analysis of the films was carried out using energy dispersive X-ray spectrometer (Quantax-200) attached to the FESEM. The thickness and optical constants of the films were estimated using spectroscopic ellipsometry (Horiba Jobin Yvon-MM16). Lateral FESEM measurements were also used to find out the thickness of the films. The transmittance spectra were recorded using UV-visible double beam spectrometer (JASCO V-550) in the spectral region 200-900 nm. The photoluminescence spectra were recorded using Flourolog III modular spectroflourometer (Horiba Jobin Yvon) equipped with a photomultiplier tube (Hamamatsu R928-28). The spectra were recorded using an excitation radiation of wavelength 325 nm from a Xe-flash lamp.

3 Results and Discussion

3.1 Structural Analysis

3.1.1 XRD Analysis

Fig. 1 shows the XRD patterns of the ZnO films (W1, W2 and W3) deposited at three different RF powers viz. 100, 150 and 200 W. The diffraction peaks observed in the XRD patterns of all the films can be

indexed to the hexagonal wurtzite phase of ZnO [JCPDS-75-0576]. The XRD pattern of the W1 film presents an intense peak at 2θ = 34.93˚ and a weak peak at 2θ = 63.58˚ corresponding to the respective lattice reflection planes (002) and (103) of the hexagonal wurtzite phase of ZnO. The high intensity of the XRD peaks exhibited by the W1 film shows its good crystalline quality. An enormous enhancement in the intensity of the XRD peak can be seen for the W2 film compared to that for the W1 film. The XRD pattern of the W2 film presents a very intense peak at 2θ = 34.93˚, two medium intensity peaks at 2θ values 36.79˚ and 63.46˚and weak peaks at 2θ values 48.01˚ and 57.28˚. These peaks can be indexed respectively to (002), (101), (103), (102) and (110) lattice reflection planes of hexagonal wurtzite ZnO phase. The XRD pattern of the W3 film presents an intense peak at 2θ = 34.97˚ and a weak peak at 2θ = 63.66˚ corresponding respectively to (002) and (103) lattice reflection planes of hexagonal wurtzite ZnO phase. No diffraction peak corresponding to metallic zinc or any other impurities are detected within the diffraction limit.

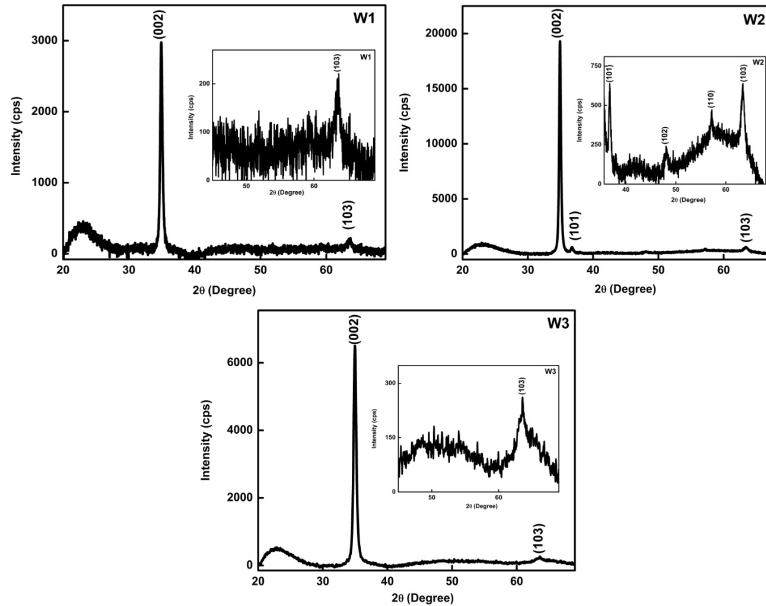

Figure 1: XRD patterns of the ZnO films (W1, W2 and W3) deposited at three different RF powers viz. 100, 150 and 200 W

XRD patterns of all the films show the highest intensity for the (002) peak. Thus all the three films present a textured nature with preferred orientation of crystal growth along c-axis. The (002) peak originates from the diffraction from the basal ZnO planes in which the grains are oriented with c-axis perpendicular to the substrate surface [Puchert et al., 1996]. The surface free energy is found to be the smallest for the (002) direction in ZnO and hence crystallites in the film prefers to grow along the c-axis [Fujimura et al., 1993, Deng et al., 2004]. The appearance of the sharp and very intense diffraction peaks in the XRD patterns indicates good crystalline quality of the as-deposited films. The intensity of the (002) diffraction peak in the XRD patterns of the W2 and W3 films are respectively about 6.6 and 2.2 times that of the W1 film (Fig. 2(a)). The variation of the full width at half maximum (FWHM) of the (002) peak as a function of RF power is also shown in Fig. 2 (a). The very high intensity and low values of FWHM of the intense (002) peak and appearance of additional peaks in the XRD pattern of the W2 film suggests its superior crystalline quality compared to others.

A slight reduction in crystallinity is observed for the W3 film compared to that of the W2 film. At high values of RF power, the Ar ions may get higher energy to bombard with the sputtering target resulting in the production of sputtered atoms with sufficient energy for the nucleation and growth of well-crystalline films on the substrate [Zhang et al., 2008]. At very high values of RF power, the sputtered particles will have very high kinetic energy and may get rebounded while colliding with the substrate and hence, may not be able to reach the equilibrium positions during film growth [Zhang et al., 2012]. The excess kinetic energy of the sputtered particles increases the probability of collisions among them leading to enhanced atomic scattering and thereby reducing the crystalline quality [Zheng et al., 2014]. Reddy et al. also suggested that higher sputtering power may induce faster reaction rate and surface damage, resulting in a reduction in the crystalline quality [Reddy et al., 2012]. The bombardment of sputtered species with excess energy will also introduce surface defects in the films leading to the reduction in crystalline quality of the films. Sputtered species reaching the substrate with high energies can either be implanted or kick surface atoms deeper in to the film [Kappertz et al., 2002].

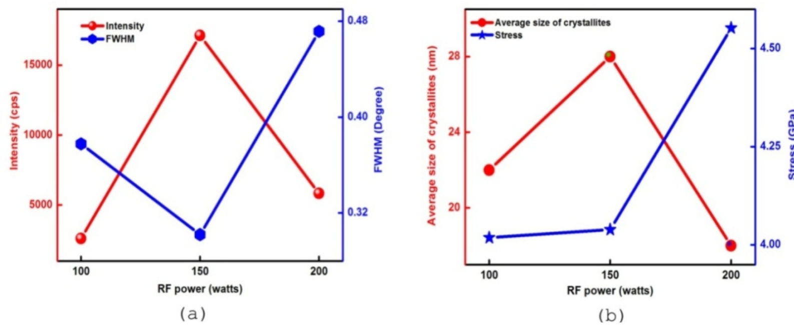

Figure: 2(a) Variation of the intensity and FWHM of the (002) peak as a function of RF power.
(b) Variation of the average size of the crystallites and stress as a function of RF power.

The average size of the crystallites in the films is determined using the Scherrer's formula, [Cullity1978, Maniv et al.,1982];

$$D_{hkl} = \frac{0.9\lambda}{\beta_{hkl}\cos\theta_{hkl}} \qquad (1)$$

where λ is the wavelength of Cu $K\alpha_1$ radiation (1.5406 Aº), β_{hkl} is the FWHM (in radian) of the most intense (002) diffraction peak and θ_{hkl} is the angle of diffraction of the peak. The average size of the crystallites estimated are found to be in the range 18-28 nm (Table. 1) and this reveals the nano-structured nature of the films. The inter planar distance 'd_{hkl}' corresponding to the prominent peaks in the films are calculated from the experimental data using Bragg's law [Cullity,1978];

$$n\lambda = 2d\sin\theta \qquad (2)$$

where λ is the wavelength of Cu $K\alpha_1$ radiation and θ is the angle of diffraction. The calculated values for 'd_{hkl}' are given in Table 2A.1. The lattice constants 'a' and 'c' for the hexagonal crystal structure can be evaluated using the following formula [Cullity,1978];

$$\frac{1}{d_{hkl}^2}=\frac{4}{3}\left(\frac{h^2+hk+k^2}{a^2}\right)+\frac{l^2}{c^2} \quad (3)$$

where 'h', 'k' and 'l' are the miller indices of the planes and 'd_{hkl}' is the inter planar distance. The calculated values of the lattice constants 'a' and 'c' are given in Table. 1. These values are close to the reported values. The strain along the c-axis (ε) is calculated using the following equation [Puchert et al.,1996, Wang et al.,2015] and the calculated values are given in Table 1.

$$\varepsilon=\left(\frac{c-c_0}{c_0}\right)\times 100\% \quad (4)$$

In the case of ZnO film, the strain along the c-axis (ε) and the biaxial stress (σ) are related by the modulus of elasticity by the Hoffman's relation [Hoffman et al.,2003, Jie et al.,2010, Kittel et al.,2005];

$$\sigma=\left[2c_{13}-(c_{11}+c_{12})\left(c_{33}/c_{13}\right)\right]\varepsilon \text{ G Pa} \quad (5)$$

where c_{ij} are the elastic stiffness constants. The values of c_{ij} for ZnO are C_{11}=209.7 GPa, C_{12}= 121.1 GPa, C_{13}=105.1 GPa and C_{33}=210.9 GPa [Hoffman et al.,2003]. Substitution of these values in equation (2A.5) leads the relation

$$\sigma=-453.6\varepsilon \text{ G Pa} \quad (6)$$

In the present case, the stress in the films is tensile in nature (Table.1) [Malek et al.,2014, Mohanty et al.,2009,Puchert et al.,1996]. The variations of average size of the crystallites and stress in the films with RF power are shown in Fig. 3(b). The films deposited at higher values of sputtering power are found to have more stress compared to those deposited at lower sputtering power (Table 1).

Sample	2θ value of (002) diffraction peak (˚)	Average crystallite size (nm)	d_{hkl} (nm)		Lattice constants (nm)		Stress (GPa)	RMS Surface Roughness (nm)
			d_{002}	d_{103}	a	c		
W1	34.93	22	0.257	0.147	0.326	0.515	4.02	2.3
W2	34.93	28	0.257	0.147	0.325	0.515	4.04	6.4
W3	34.97	18	0.257	0.147	0.327	0.514	4.55	7.8

Table 1: Structural and morphological parameters of the ZnO films deposited at various sputtering powers

The biaxial stress in thin films can mainly be of two types; intrinsic stress and extrinsic stress. The intrinsic stress is generally correlated to the defects and impurities in the films whereas the extrinsic stress is linked with lattice mismatch between the substrate and film and the mismatch in thermal expansion coefficients (TEC) of the substrate and film [Li et al.,2007]. The strain in the films developed due to the lattice mismatch may get relieved at the growth temperature via dislocation formation [Vincent et al., 1969]. Strain can be developed in the films due to the difference in the values of thermal expansion coefficients of the film and the substrate [Srikant et al.,1997]. Srikant et al. suggested that if the substrate is much thicker than the film, then the substrate is essentially stress-free and the strain has to be borne by the film itself [Srikant et al.,1997]. Since, the lateral dimensions of a film are much larger than its thickness; the film is under a plane stress condition [Srikant et al.,1997]. The extrinsic stress in the films is given by;

$$\sigma_{ext} = \sigma_{th} + \sigma_{latt} \tag{7}$$

where σ_{th} and σ_{latt} are the stresses due to thermal mismatch and lattice mismatch respectively. Here, the films are deposited on quartz substrate. The calculation of the value of stress introduced by lattice mismatch between ZnO film and quartz is difficult because of the amorphous nature of quartz [Mohanty et al.,2009, Li et al.,2007]. The thermal expansion coefficient of ZnO ($2.9\times10^{-6}/K$) is much larger than that of the fused quartz substrate ($0.59\times10^{-6}/K$). This may produce a residual stress in the film due to the rise in temperature during sputtering [Kappertz et al.,2002, Singh et al.,2015]. The stress introduced due to the difference in TEC values of film and substrate is given by the following equation [Li et al.,2007];

$$\sigma_{th} = \int_{T_{growth/anneal}}^{RT} \left(\alpha^{s} - \alpha^{b}\right)\frac{E}{1-\eta}\,dT \tag{8}$$

where α^{s} and α^{b} are respectively the TEC values of the substrate and the bulk material. E and η are respectively the Young's modulus and Poissons ratio of the material. In the present case, $\alpha^{s} = 0.59\times10^{-6}/K$ (for quartz substrate) and $\alpha^{b} = 2.9\times10^{-6}/K$ (for ZnO) and Young's modulus and Poisson's ratio for ZnO are $E = 100$ GPa and $\eta = 0.36$ [Kappertz et al.,2002, Singh et al.,2015, Malek et al.,2014]. The electron impact on the substrate produces substrate heating during sputtering process. Even though the sample is not heated externally, due to energy flux during sputtering process there will be rise in temperature. The highest value of temperature measured using thermocouple during sputtering process is below 100ºC. Taking this as an upper limit for the rise in substrate temperature, the thermal stress calculated for the films is ~0.026 GPa, which is much less than the total stress in the films. This implies that the intrinsic stress can be the main source of the stress in the films.

In sputtering, stress is developed in the film due to the implantation of sputtered particles from the oxide target into the growing film [Mohanty et al.,2009]. During sputtering of oxide target, the surface oxygen gets easily ionized and these negative ions are accelerated by the electric field and reach the substrate with sufficient energy for implantation [Kappertz et al.,2002]. Although, during their transit, these ions are neutralized, they reach the substrate with sufficient energy for implantation. This bombardment and implantation of particles sputtered from the target into the growing film introduce stress in the deposited film [Mohanty et al.,2009, Kappertz et al.,2002].

3.1.2 Raman Spectroscopic Analysis

According to Group theory, hexagonal wurtzite ZnO has space group c_{6v}^{4} (p6$_3$mc and z=2). All the Zn and O atoms occupy the C_{3v} sites. The 9 optical phonon modes at the centre of the Brillouin zone is given by [Fateley-1972];

$$\Gamma_{opt} = A_1 + 2B_1 + E_1 + 2E_2. \quad (9)$$

Among these modes, A_1, E_1 and E_2 modes are Raman active, A_1 and E_1 modes are IR active and B1 mode is inactive in both IR and Raman spectra. The polar A_1 and E_1 modes split into TO and LO modes. TO means transverse optical and LO means longitudinal optical. The A_1 phonon mode is polarized parallel to the c-axis, whereas the E_1 phonon mode is polarized perpendicular to the c-axis [Yahia et al., 2008].

The Raman spectra of the ZnO films are shown in Fig. 3(a)-(c). All the three films present bands ~100 and 437 cm^{-1} with appreciable intensity corresponding to $E_2(Low)$ and $E_2(High)$ modes of hexagonal wurtzite ZnO phase respectively. The $E_2(Low)$ and $E_2(High)$ modes are associated respectively to the vibrations of heavy Zn-sublattice and oxygen atoms. $E_2(High)$ mode is the characteristic feature of hexagonal wurtzite ZnO [Li et al.,2012]. The presence of strong $E_2(High)$ mode in the Raman spectrum of ZnO is an indication of its good crystalline quality. The plot showing the variation of FWHM of the $E_2(High)$ mode with sputtering power is given in Fig. 3(d). The film deposited at an RF power of 150 W shows the least value of FWHM. This indicates its good crystalline quality compared to others. The $E_1(LO)$ mode is observed ~ 584 cm^{-1} in the films. The $E_1(LO)$ mode originates from defects such as oxygen vacancies, interstitial zinc or their complexes or other defect states [Yahia et al.,2008, Zhang et al.,2009]. The weak band observed ~333 cm^{-1} can be attributed to $E_2(High) - E_2(Low)$ mode. The band observed ~ 488 cm^{-1} may have the contribution from the quartz substrate. The weak band observed ~ 275 cm^{-1} in the Raman spectra of the films can be due to the activation of silent modes [Calleja et al.,1977, Tzolov et al.,2000, Mcguire et al.,2002].

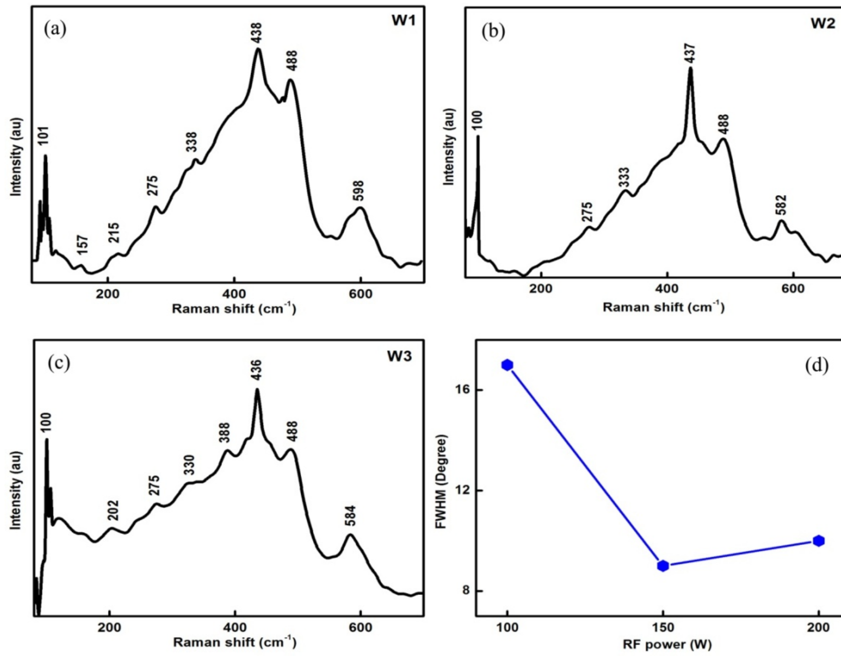

Figure: 3 (a)-(c). Micro-Raman Spectra of (a) ZnO films deposited at RF powers 100,150 and 200W and (d) Variation of FWHM of E2(High) mode as a function of sputtering power.

The stress in the film can affect the position of the $E_2(High)$ mode. In the films under compressive stress, the $E_2(high)$ mode undergoes a blue shift in its position, whereas in the films under tensile stress, the $E_2(high)$ mode shows a red shift [Huang et al.,2003, Li et al.,2012, Ben et al.,2008, Decremps et al.,2002]. With increase in RF power, a systematic decrease in the position of $E_2(high)$ mode can be observed. From XRD analysis, higher values of tensile stress are observed in films fabricated at higher RF powers.

3.2 Surface morphology and Elemental Analysis

3.2 .2 AFM Analysis

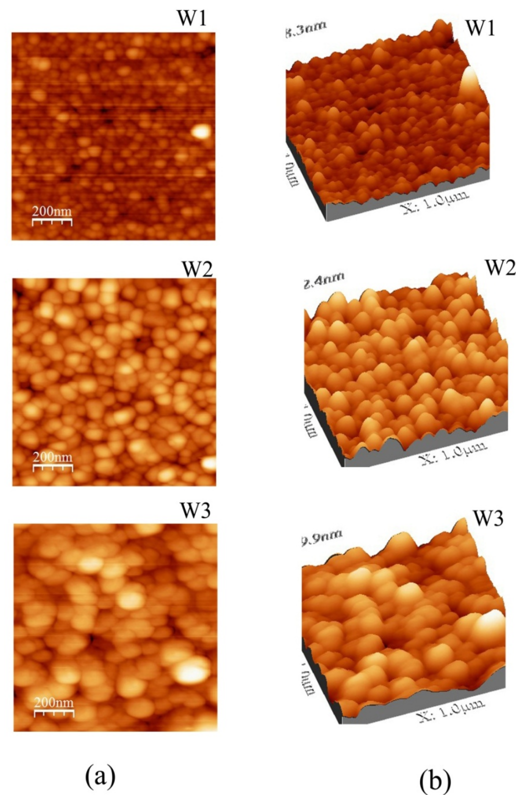

Figure: 4. (a) 2D and 3D AFM Micrographs of ZnO films deposited at RF powers 100,150 and 200W.

The 2D and 3D AFM micrographs of the ZnO films sputtered at different RF powers viz 100, 150 and 200 W are shown in Fig. 4 (a) and (b) respectively. All the films present well-defined grains which are densely distributed over the surface. A systematic improvement in the size of the grains as a function of RF power can be seen from the AFM images. The analysis of the grain size and RMS surface roughness of the films is carried out using WSxM 5.0 Develop 6.4 software. The W1 film consists of grains of average size in the range 50-60 nm. The W2 film consists of grains of average grain size in the range 70-100 nm. The W3 film presents grains of size distribution in the range 80-120 nm. A systematic increase in the value of RMS surface roughness is observed (Table.1) with increase in RF power.

As the RF power increases more and more energetic particles may reach the substrate surface, the deposition of which may induce higher surface roughness [Kim et al.,2000]. Smooth film with smaller particles of uniform size distribution is formed in the film deposited at lower sputtering power of 100 W. As the RF power increases more and more energetic particles sputtered from the target surface impinge on the substrate resulting in the formation of larger grains with higher RMS surface roughness. Sayago et al. suggested that higher sputtering power provides higher energy to surface atoms resulting in the oriented crystal growth with higher RMS surface roughness values [Sayago et al.,2004].

3.2 .2 FESEM and EDX Analysis

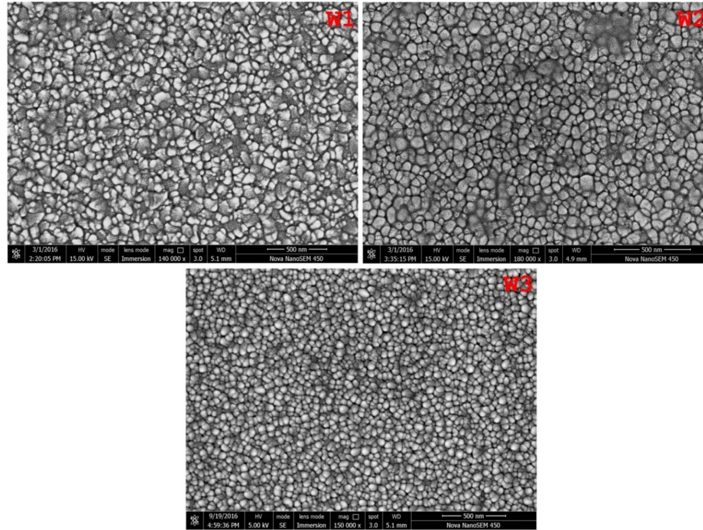

Fig.5 FESEM images of ZnO films deposited at RF powers 100, 150 and 200 W.

Fig.5 shows the FESEM micrographs of the ZnO films sputtered at different RF powers viz 100, 150 and 200 W. All the films present dense uniform distribution of grains similar to that observed in the AFM micrographs.

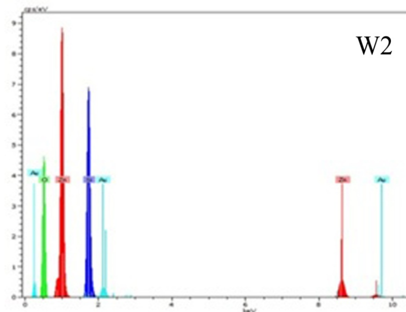

Figure: 6 Typical EDX Spectrum of ZnO film deposited at an RF power of 150 W.

The EDX spectral pattern of ZnO film (W2) shows peaks corresponding to Zn, O, Si and Au elements (Fig. 6). The observation of peaks corresponding to Zn and O reveal the formation of ZnO. Since the films are deposited on the quartz substrate, the Si peak has its origin from the substrate contribution. The films for FESEM analysis are coated with gold (Au) to improve its electrical conductivity and the Au peaks in the EDX spectrum originates from the surface coating.

Lateral FESEM measurements (Fig. 7 (a)) were used to find out the film thickness. A systematic

improvement in the film thickness with increase in RF power is observed from the lateral FESEM analysis. The variation of the film thickness as a function of RF power is shown in Fig. 7 (b). As the RF power increases, more and more energetic particles may reach the substrate and this may result in the improved deposition rate. The improvement in thickness with raise in RF power can be due to the enhanced deposition rate.

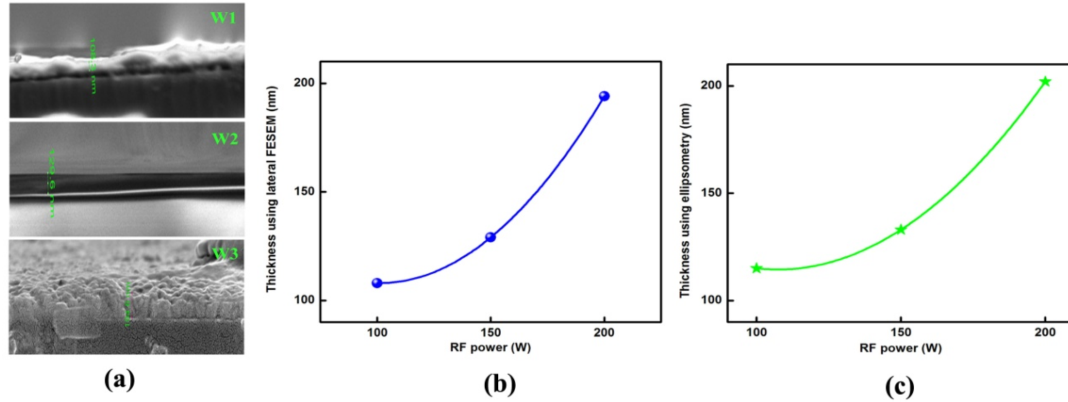

Figure: 7. (a) Lateral FESEM Micrographs of ZnO films deposited at RF powers 100,150 and 200W showing the thickness (b) and (c) Variations of thickness of the film as a function of RF power for these films estimated by lateral FESEM measurements and spectroscopic ellipsometry.

3.3 Optical Properties

3.3.1 Spectroscopic Ellipsometric Analysis

The optical constants and thickness of the films are determined indirectly using spectroscopic ellipsometry. The polarization change can be measured using the ellipsometric angles Ψ and Δ corresponding to the amplitude ratio and relative phase change respectively. A linearly polarized incident beam is converted to an elliptically polarized reflected beam. The polarization ellipsoid is defined by p (parallel to the plane of incidence) and s (perpendicular to the plane of incidence) co-ordinate system [Logothetidis et al.,2008]. The ellipsometric equation is given by [Yang et al.,2009],

$$\rho = \frac{r_p}{r_s} = \tan(\Psi)e^{i\Delta} \tag{10}$$

where r_p and r_s represents Fresnel reflection coefficients of the sample. The spectroscopic ellipsometric data is analyzed by Delta-Psi software. The measured data are fitted to a suitable model to extract the information about the optical constants and thicknesses of the films. To fit the experimental data with the theoretical model, an optical model of the measured sample is constructed. It consists of three layers. The base layer is the substrate on which the thin film is deposited. Middle layer consists of a dense film of ZnO and the top layer consists of porous ZnO film. Void is also included in the first layer to account the effect of surface roughness. The model used for fitting the measured data is an analytical dispersion function of complex refractive index or permittivity. The fitting process is carried out in such a way that χ^2, the square of the statistical difference between the experimental values (from the measured data) and calculated values (from the model) is a

minimum. The Cauchy model is generally used for fitting the experimental data of ZnO films as its exponential absorption tail may describe the sub-band gap absorption at the band gap edge very well. In the Cauchy model refractive index is described as a slowly varying function of wavelength given by the following equation,

$$n(\lambda) = A + \frac{B}{\lambda^2} + \frac{C}{\lambda^4} \tag{11}$$

where A, B and C are the Cauchy coefficients for given material [Jan et al.,2011]. The spectral fitting with the Cauchy model is shown in Fig. 8(a). The dependence of refractive index and dielectric constants on the incident wavelength for the films are shown in Fig. 8(b) and (c) respectively.

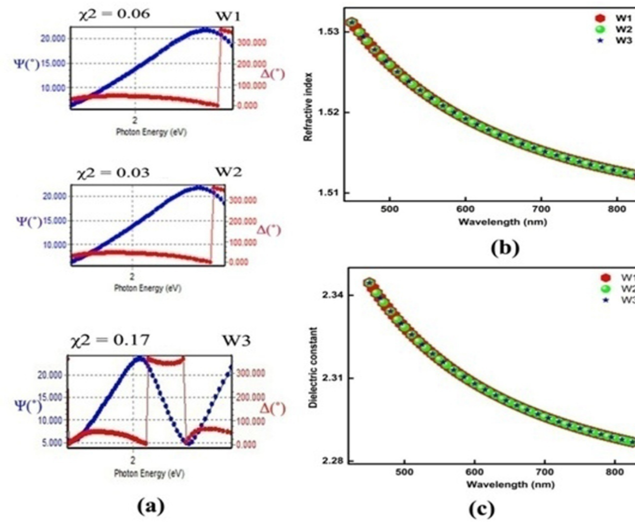

Figure: 8(a) Fitted curves of ellipsometric data using Cauchy model. (b) and (c) The variation of real part of refractive index and dielectric constant respectively as a function of RF power.

For all the films, the refractive index and dielectric constant follows normal dispersion behaviour. The values of the refractive index and dielectric constants of the films at the wavelength 550 nm is given in Table 2.The values of thickness obtained from spectroscopic ellipsometry agree well with the film thickness values obtained from lateral FESEM images.

3.3.2 UV-Visible Spectral Analysis

Fig.9 (a) and (b) shows the transmittance and reflectance spectra of the ZnO films prepared at RF powers 100, 150 and 200 W. The average values of transmittance are estimated for all the films in the wavelength region 400-900 nm (Table 2). The very high transmittance exhibited by the films can be attributed to their high degree of crystallinity revealed by the earlier analyses. The film deposited at an RF power of 150 W shows the highest value of transmittance, which can be due to its superior crystalline quality compared to others as revealed by the XRD, Raman, AFM and FESEM analyses. The transmittance of the films show a sharp fall ~ 390 nm due to the fundamental absorption of ZnO corresponding to its intrinsic band edge.

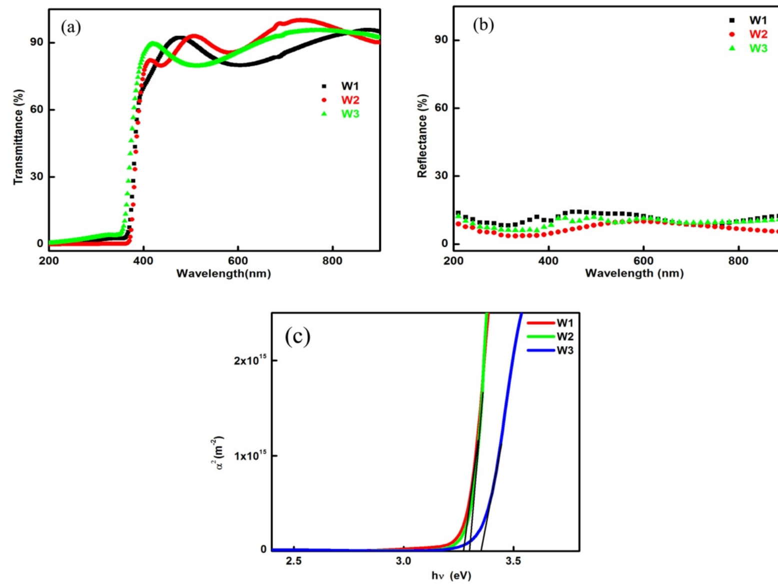

Figure: 9 (a) Transmittance spectra (b) Reflectance spectra and (c) Plot of α2 vs hυ for the ZnO films deposited at RF powers 100, 150,200 W.

The optical absorption coefficient α can be obtained from the transmittance data using the formula;

$$\alpha = \frac{1}{t}\ln\left(\frac{1}{T}\right) \tag{12}$$

where T is the transmittance and t is the thickness of the sample.
The optical band gap energy of the films can be determined using the following relation;

$$\alpha(h\nu) = A\left(h\nu - E_g\right)^n \tag{13}$$

where h is the Planck's constant, ν is the frequency of incident photon, E_g is the bandgap corresponding to a particular transition, A is the band edge constant depending on electron-hole mobility and 'n' determines the nature of transition. n can have values $\frac{1}{2}$, $\frac{3}{2}$, 2 or 3 depending on the case whether the transition is direct allowed, direct forbidden, indirect allowed or indirect forbidden [Goswami et al.,1996, Pankove et al.,1971, Rani et al.,2006, Lethy et al.,2008]. It is found that the best fit is observed for $n = \frac{1}{2}$ for all the films indicating direct band gap nature of the films. The band gap energy of the direct band gap semiconductor can be calculated by plotting α^2 versus hν and extrapolating the linear region of the plot to zero absorption (α = 0). The band gap energy calculations of these films show that the band gap values are ~3.3 eV (Table 2) [Fig. 9 (c)].

3.3.3 Photoluminescence Spectroscopy

The photoluminescence spectra of the films recorded with an excitation wavelength of 325 nm are shown in Fig.10. All the films show a broad emission band extending from 360-460 nm. Among the three films, the W2 film shows the highest intensity for PL emission. In the PL spectra of ZnO, usually the near band edge emission due to the recombination of holes in the valance band (VB) with electrons from the conduction band (CB) occurs in the UV region ~ 390 nm wavelength. During the process of film preparation a lot of defects may occur in the film. These defects may introduce new levels in the forbidden region between the VB and the CB. These defect level transitions may yield visible PL emissions. In good quality films one can expect intense UV emission due to NBE emission in ZnO. For a detailed analysis, the PL spectra of the films were deconvoluted. All the PL spectra yield two distinct peaks at ~395 and 425 nm. The peak observed ~ 395 nm (3.14 eV) corresponds to the near band edge (NBE) emission in ZnO. The peak position of this UV emission is in accordance with the peak position of the typically reported free excitonic transition in ZnO [Zu et al.,1997, Cho et al.,1997, Li et al.,2006-1]. Zheng et al. suggested that strong UV emission from ZnO films indicates good crystal quality of the films [Zheng et al.,2011].

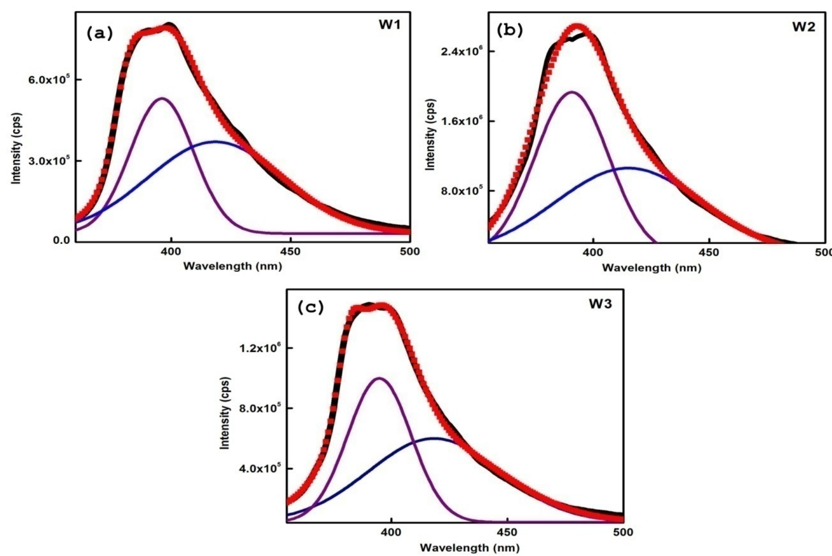

Figure: 10 Deconvoluted photoluminescence spectra of the ZnO films deposited at different rf powers 100, 150 and 200w.

Sun et al. has calculated the energy levels of the intrinsic defects in ZnO using full-potential linear muffin-tin orbital method [Sun et al.,2000, Xu et al.,2001]. The energy interval from interstitial zinc (Zn_i) level to the top of the VB is about 2.9 eV and hence, the observed blue emission ~ 425 nm can be attributed to the interstitial zinc related defects. The comparison of the relative intensity of the NBE emission and defect level emissions give an idea of the crystalline quality of the films. The W2 film shows highest intensity for UV emission which can be attributed to its superior crystalline quality compared to others as revealed from the structural analysis.

4 Conclusions

ZnO films were prepared on quartz substrate using different RF powers (100, 150 and 200 W). The effect of RF power on structural, morphological, optical and luminescent properties of ZnO films were investigated. Good crystalline, c-axis oriented films with hexagonal wurtzite phase are obtained in all cases. The lowest value of FWHM and the highest value of intensity for the main XRD peak for the film deposited at an RF power of 150 W suggest that, 150 W is the optimum RF power for fabricating good crystalline ZnO films. The surface morphology of the films presents a very dense, uniform distribution of grains with well-defined grain boundary. A very high transmittance is observed for these films in the visible region. The PL spectra of the films present an intense UV-emission due to NBE transition and a visible emission due to zinc interstitial defects in ZnO.

References

1. S.B. Yahia, L.Znaidi, A.Kanaev and J.P.Petitiet, Spectrochim. Acta, Part A71 (2008) 1234-1238.
2. B.D. Cullity & S.R. Stock, Elements of X-ray diffraction, 3rd Edition, MA: Addison-Weseley; 1978, Chapter 5, Diffraction III: Real Samples.
3. Frede´ric Decremps, Julio Pellicer-Porres, A. Marco Saitta, Jean-Claude Chervin and Alain Polian, Physical Review B, volume 65(2002) 092101.
4. W.G. Fateley, F.R. Dollish, N.T. Mc Devitt and F.F. Bentley, Infrared and Raman Selection Rules for Molecular and Lattice Vibrations-The Correlation Method,Wiley-Interscience, New York, 1972.
5. A. Goswami, Thin Film Fundamentals, New Age International (p) Limited, New Delhi, 1996.
6. R. L. Hoffman, B. J. Norris, and J. F. Wagner, Appl. Phys. Lett. 82 (2003) 733;
7. Y. Huang, M. Liu, Z. Li, Y. Zeng and S. Liu, Mater. Sci. Eng. B. 97 (2003) 111-116; doi: 10.1016/S0921-5107(02)00396-3
8. Litty Irimpan, V.P.N.Nampoori and P. Radhakrishnan, J. Appl. Phys. 104 (2008) 113112–113115; doi:10.1063/1.3032897.
9. .J. Gooch Encyclopedic Dictionary of Polymers, 2nd edition Springer New York (2011) p.125; doi:10.1007/978-1-4419-6247-8-2056.
10. J. Jie, A. Morita and H. Shirai, J. Appl. Phys. 108 (2010) 033521; doi:10.1063/1.3457867
11. O. Kappertz, R. Drese and M. Wuttig, J. Vac. Sci. Technol. A 20(6) (2002) 2084-2095; doi: 10.1116/1.1517997
12. Y. Kashiwaba, K. Sugawara and K. Haga, Thin Solid Films, 411 (2002) 87-90.
13. Y. Kashiwaba, K. Sugawara and K. Haga, Thin Solid Films, 411 (2002) 87-90.
14. K. K. Kim, J.H. Song, H.J. Jung, W.K. Choi, S.J. Park, J.H. Song and J.Y. Lee, J. Vac. Sci. Technol. A 18

(2000) 2864; doi: 10.1116/1.1318192

15.C. Kittel, Introduction to Solid State Physics, 8th ed. (John Wiley & Sons, Inc., New York, 2005), p. 82.

16.H.J. Ko, Y.F. Chen and Z. Zhu, Appl. Phys. Letters, 76 (2000) 1905-1907

17.Krunks, A. Katerski, T. Dedova, I. Oja Acik and A. Mere, Sol. Energy Mater. Sol. Cells, 92 (2008) 1016-1019; doi:10.1016/j.solmat.2008.03.002

18.Malle Krunks, Enn Mellikov, Thin Solid Films 270 (1995) 33-36;
doi: 10.1016/0040-6090(95)06893-7

19.K.J. Lethy, D. Beena, R. Vinodkumar and V.P. Mahadevan Pillai, Appl. Surf. Sci. 254 (2008) 2369.

20.C. Li, G.J. Fang, F.H. Su, G.H. Li, X.G. Wu and X.Z. Zhao, Nanotechnology 17 (2006) 3740.

21.Y. F. Li, B. Yao, Y. M. Lu, C. X. Cong, Z. Z. Zhang, Y. Q. Gai, C. J. Zheng, B. H. Li, Z. P. Wei, D. Z. Shen, X. W.Fan, L. Xiao, S. C. Xu and Y. Liu, Appl. Phys.Lett. 91 (2007) 021915; doi: 10.1063/1.2757149.

22.W.J. Li, C.Y. Kong, H.B. Ruan, G.P. Qin, G.J. Huang, T.Y.Yang, W.W. Liang, Y.H. Zhao, X.D. Meng, P. Yu, Y.T. Cui and L. Fang, Solid State Commun. 152 (2012) 147-150; doi:10.1016/j.ssc.2011.10.006

23.S. Logothetidis, A. Laskarakis, S. Kassavetis, S. Lousinian,C. Gravalidis and G. Kiriakidis, Thin Solid Films. 516, 2008, 1345-1349; doi:10.1016/j.tsf.2007.03.171

24.Y.M. Lua, W.S. Hwang, W.Y. Liu and J.S. Yang, Mater. Chem. Phys. 72 (2001) 269-272.

25.S. Maniv, W.D. Westwood and E. Colombini, J. Vac. Sci. Technol. 20 (1982) 162.

26.M.F. Malek, M.H. Mamat, Z. Khusaimi, M.Z. Sahdan,M.Z. Musa, A.R. Zainun, A.B. Suriani, N.D. Md Sin, S.B. Abd Hamid and M. Rusop, J. Alloys and Compounds 582 (2014) 12-21; doi:10.1016/j.jallcom.2013.07.202

27.A. V. Maslov, and C. Z.Ning, Opt. Lett. 29 (2004) 572.

28.K. Mcguire, Z. W. Pan, Z. L. Wang, D. Milkie, J. Menéndez and A. M. Rao, J. Nanosci. Nanotech. 2 (2002) 1-4.

29.B. C.Mohanty, Y. H. Jo, D. Ho Yeon, Ik Jin Choi and Y. S. Cho, Appl. Phys. Lett. 95 (2009) 062103; doi: 10.1063/1.3202399.

30.Y. Natsume, H. Sakata, Thin Solid Films, 372 (2000) 30-36.

31.T.Ohshima, R.K.Thareja, T.Ikegami and K.Ebihara, Surf. Coat. Technol. 169-170 (2003) 517-520.

32.J. Pankove, Optical Process in Semiconductors, Dover Publication, New York, 1971.

33.S. Pati, P. Banerji and S.B. Majumder, Sensors and Actuators A 213 (2014) 52-58.

34.M. K. Puchert, P. Y. Timbrell, R. N. Lamb, J. Vacuum Science & Technology A, 14 (1996) 2220; doi: 10.1116/1.580050.

35.J.R. Rani, V.P. Mahadevan Pillai, R.S. Ajimsha, M.K. Jayaraj and R.S. Jayasree, J. Appl. Phys. 100 (2006) 014302

36.R. Subba Reddy, A. Sivasankar Reddy, B. Radhakrishna, S. Uthanna, Cryst. Res. Technol. 47, No. 10 (2012)1095-1104; doi: 10.1002/crat.201200150.

37.Y. R. Ryu, S. Zhu, J. D. Budai, H. R. Chandrasekhar, P. F. Miceli and H. W. White, J. Appl. Phys. 88 (2000) 201; doi: 10.1063/1.373643.

38.I.Sayago, M.Aleixandre, L. Ares, M. J. Fernández, J. R. Santos, J Gutiérrez and M. C. Horrillo, 245-1 (2004) 273-280; doi:10.1016/j.apsusc. 2004.10.035.

39.J. Singh, S. Ranwa, J. Akhtar and M. Kumar, AIP Advances 5, 2015, 067140-8.

40.V. Srikant and D. R. Clarke, J. Appl. Phys., Vol. 81, No. 9, (1997) 6357-6364.

41.M. Tzolov, N. Tzenov, D. Dimova-Malinovska, M. Kalitzova, C. Pizzuto,G. Vitalic, G. Zolloc and I. Ivanov, Thin Solid Films 379 (2000) 28-36.

42.M.Wang and L. Zhang, Materials Letters 63 (2009) 301-303; doi:10.1016/j.matlet.2008.10.022

43.Y. Wang, W. Tang, J. Liu, L. Zhang, Appl. Phys. Lett.106 (2015) 162101; doi: 10.1063/1.4918933

44.W. Xu, Z. Ye, T. Zhou, B. Zhao, L. Zhu and J. Huang, J. Crystal Growth 265 (2004) 133-136; doi:10.1016/j.jcrysgro.2003.12.061

45.L.Yang, Y.H.Tang, A.P.Hu and L.D. Zhang, Physica B, 403 (2008) 2230-2234; doi:10.1016/j.physb.2007.12.013

46. W.H.Zhang, J.L.Shi, L.Z.Wang and S.S.Yan, Chem.Mater.12 (5) (2000) 1408–1413; doi: 10.1021/cm990740a.

47. S. B. Zhang, S. H. Wei and A. Zunger, Phys. Rev. B, 63(2001) 075205; doi: 10.1103/PhysRevB.63.075205

48. D.H. Zhang, Q.P. Wang and Z.Y. Xue, Appl. Surf. Sci. 207 (2003) 20-25; doi:10.1016/S0169-4332(02)01225-4

49. J.H. Zheng, Q. Jiang, J.S. Lian, Appl. Surf. Sci. 257 (2011) 5083-5087; doi:10.1016/j.apsusc.2011.01.025

50. Y. Zheng, Q. Liang, B. Li, G. Zeng, W. Wang, J. Zhang, W. Li and L. Feng, Adv Mat Res, 1058 (2014) 240-243.

51. P. Zu, Z.K. Tang, G.K.L. Wong, M. Kawasaki, A. Ohtomo, H. Koinuma and Y. Segawa, Solid State Commun. 103 (1997) 459-463; doi:10.1016/S0038-1098(97) 00216-0.